

Hemodynamic Deconvolution Demystified: from Paradigm Free Mapping to Total Activation

Eneko Uruñuela^{a,b,*}, Thomas A.W. Bolton^{c,d}, Younes Farouj^d, Dimitri Van de Ville^{d,e}, César Caballero-Gaudes^a

^a*Basque Center on Cognition, Brain and Language (BCBL), Donostia-San Sebastián, Spain.*

^b*University of the Basque Country (EHU/UPV), Donostia-San Sebastián, Spain.*

^c*Gamma Knife Center, Department of Clinical Neuroscience, Centre Hospitalier Universitaire Vaudois (CHUV), Lausanne, Switzerland*

^d*Swiss Federal Institute of Technology Lausanne (EPFL), Lausanne, Switzerland.*

^e*Faculty of Medicine of the University of Geneva, Geneva, Switzerland*

Abstract

Deconvolution of the hemodynamic response is an important step to access short timescales of brain activity recorded by fMRI. Albeit conventional deconvolution algorithms have been around for a long time (e.g., Wiener deconvolution), recent state-of-the-art methods based on sparsity-pursuing regularization are attracting increasing interest to investigate brain dynamics. This technical note revisits the main concepts underlying two main methods, Paradigm Free Mapping and Total Activation, in the most accessible way. Despite their apparent differences, these methods are theoretically equivalent as they represent the synthesis and analysis sides of the same problem. We demonstrate this equivalence in practice with their best-available implementations using both simulations, with different signal-to-noise ratios, and experimental data of motor task and resting-state fMRI. We evaluate the parameter settings that lead to equivalent results, and benchmark the computational speed of both algorithms. This note is useful for practitioners interested to better understand state-of-the-art hemodynamic deconvolution, and want to make use of the most efficient implementation.

Keywords: fMRI deconvolution, paradigm free mapping, total activation

1. Introduction

Functional magnetic resonance imaging (fMRI) data analysis is often directed to disentangling and understanding the neural processes that occur among brain regions.

While interactions in the brain are electrical in nature, the blood oxygenation level-dependent (BOLD) signal present in fMRI data reflects hemodynamics. Thus, an intermediate step that estimates the underlying neuronal activity from the BOLD signal can prove to be useful for understanding such interactions. Often, the analysis of task fMRI data relies on general linear models (GLM) to detect maps of brain activity by using the information about the timings of the BOLD events. However, this information can be unknown, inaccurate, or insufficient in some scenarios. In such cases, and given the nature of the BOLD signal, the appropriate approximation of the neuronal activity can be obtained by means of deconvolution with an assumed hemodynamic response (Gitelman et al. 2003).

Deconvolution and methods alike are becoming more popular for exploring time-varying activity in fMRI data within a number of neuroimaging studies due to their potential to blindly disentangle neural dynamics. One of such cases is the study of resting-state fluctuations with

the aim of gaining insight into the origin of the signals driving functional connectivity and its temporal dynamics, as well as the organizational principles of brain function; i.e., to study and deconstruct the spatio-temporal structure of functional components that dynamically construct resting-state networks (Petridou et al. 2013; Karahanoglu and Van De Ville 2015, 2017; Kinany et al. 2020; Gonzalez-Castillo et al. 2019; Allan et al. 2015). Deconvolution techniques can also prove to be helpful in clinical conditions to characterize functional alterations of patients with a progressive stage of multiple sclerosis at rest (Bommarito et al. 2020), to find functional signatures of prodromal psychotic symptoms and anxiety at rest on patients suffering from schizophrenia (Zöller et al. 2019), to detect the foci of interictal events in epilepsy patients without an EEG recording (Lopes et al. 2012), or to study functional dissociations observed during non-rapid eye movement sleep that are associated with reduced consolidation of information and impaired consciousness (Tarun et al. 2020).

A series of recent studies have also attempted to understand neural processes by studying the interactions between BOLD responses without estimating the underlying neuronal activity. For instance, co-activation patterns have been used to replicate seed correlation-based resting-state functional networks with a small portion of the data (Liu and Duyn 2013; Liu et al. 2013, 2018; Majeed et al. 2009, 2011; Cifre et al. 2020a,b; Zhang et al. 2020). Like-

*Corresponding author

Email address: e.urunuela@bcbl.eu (Eneko Uruñuela)

wise, the dynamics of functional connectivity have recently been investigated with the use of co-fluctuations and edge-centric techniques on tasks (Faskowitz et al. 2021), resting-state (Esfahlani et al. 2020) and naturalistic paradigms (Faskowitz et al. 2020; Betzel et al. 2020). Methods based on the multiplication of temporal derivatives have also been presented for the estimation of dynamic functional connectivity on task fMRI data (Shine et al. 2015, 2016).

This note revisits synthesis- and analysis-based deconvolution methods for fMRI data and comprises four sections. In the first, we present the theory behind two state-of-the-art deconvolution approaches based on estimators that promote sparsity: Paradigm Free Mapping (PFM) (Caballero Gaudes et al. 2013) — available as *3dPFM* and *3dMEPFM* in AFNI — and Total Activation (TA) (Karahanoglu et al. 2013) — available as part of the *iCAPs toolbox*. We then assess their performance controlling for a fair comparison on simulated and experimental data. Finally, we discuss the benefits and shortcomings of the techniques and conclude with our vision on potential extensions and developments.

2. Theory

The hemodynamic response to neuronal activity can be modeled as the convolution the activity-inducing signal $s(t)$ with the hemodynamic response function $h(t)$ as $x(t) = h(t) * s(t)$ (Gitelman et al. 2003). The fMRI signal at a given voxel $y(t)$ can then be decomposed into neuronal-related hemodynamic $x(t)$ and noise components $n(t)$ as:

$$y(t) = x(t) + n(t), \quad (1)$$

which can be reformulated in matrix notation as $\mathbf{y} = \mathbf{Hs} + \mathbf{n}$, where $\mathbf{y}, \mathbf{s} \in \mathbb{R}^N$, $\mathbf{H} \in \mathbb{R}^{N \times N}$ is the HRF in Toeplitz matrix form, and N is the number of frames of the fMRI acquisition. The signal model in (1) can also be extended to represent the neuronal signal \mathbf{s} in terms of its innovation signal \mathbf{u} , i.e., its derivative, as $\mathbf{s} = \mathbf{Lu}$ where $\mathbf{L} \in \mathbb{R}^{N \times N}$ is an integration operator (Cherkaoui et al. 2019; Uruñuela et al. 2020).

Hence, the maximum likelihood estimate of the hemodynamic response to the underlying neural activity can be calculated using the ordinary least-squares estimator that minimizes the residual sum of squares between the modeled (\mathbf{Hs}) and measured (\mathbf{y}) signals. Yet, the estimates of the neuronal activity \mathbf{s} must be constrained with a regularization term to attenuate the collinearity and high variability of the design matrix \mathbf{H} .

2.1. Synthesis-based deconvolution

Synthesis-based Paradigm Free Mapping (PFM) builds upon the signal model introduced in (1); i.e., the BOLD signal is the result of convolving the underlying neural activity with the hemodynamic response, and proposes to estimate the activity-inducing signal by solving the following

regularized least-squares problem (Caballero Gaudes et al. 2013; Uruñuela et al. 2020; Gaudes et al. 2011):

$$\hat{\mathbf{s}} = \arg \min_{\mathbf{s}} \frac{1}{2} \|\mathbf{y} - \mathbf{Hs}\|_2^2 + \Omega(\mathbf{s}), \quad (2)$$

where $\Omega(\mathbf{s})$ is the regularization term.

Assuming that single-trial BOLD responses are the result of brief bursts of neuronal activation, the activity-inducing signal \mathbf{s} must be a sparse vector. Thus, sparse estimates of \mathbf{s} could be obtained by substituting $\Omega(\mathbf{s})$ in (3) with an l_0 -norm and solving the optimization problem (Bruckstein et al. 2009). However, due to the convolution model defined in (3), finding the optimal solution to the problem demands an exhaustive search across all possible combinations of the columns of the design matrix \mathbf{H} . Hence, a pragmatic solution is to solve the optimization problem with the use of an l_1 -norm, or LASSO (Tibshirani 1996), which is a convex function and therefore provides fast convergence to the optimal solution.

$$\hat{\mathbf{s}} = \arg \min_{\mathbf{s}} \frac{1}{2} \|\mathbf{y} - \mathbf{Hs}\|_2^2 + \lambda \|\mathbf{s}\|_1, \quad (3)$$

where λ regulates how sparse the optimal solution is.

Such formulation provides flexibility to expand the capabilities of PFM. For instance, incorporating the integration operator \mathbf{L} into the design matrix \mathbf{H} allows the recovery of the innovation signal \mathbf{u} ; i.e., the derivative of the activity-inducing signal \mathbf{s} . Therefore, the innovation signal can be estimated by solving the following optimization problem (Cherkaoui et al. 2019; Uruñuela et al. 2020):

$$\hat{\mathbf{u}} = \arg \min_{\mathbf{u}} \frac{1}{2} \|\mathbf{y} - \mathbf{HLu}\|_2^2 + \lambda \|\mathbf{u}\|_1. \quad (4)$$

2.2. Analysis-based deconvolution

Even though based on the same signal model as PFM, analysis-based Total Activation (TA) proposes to use a linear differential operator L_h that inverts the hemodynamic system based on activelets to recover the activity-inducing signal \mathbf{s} (Karahanoglu et al. 2013; Khalidov et al. 2011; Karahanoglu et al. 2011):

$$L_h\{x\}(t) = s(t) \quad (5)$$

where x is the neuronal-related signal; i.e., the activity inducing signal \mathbf{s} convolved with the HRF, and L_h is defined as

$$L_h = \prod_{i=1}^{M_1} (D - \alpha_i I) \left(\prod_{j=1}^{M_2} (D - \gamma_j I) \right)^{-1}, \quad (6)$$

where D is the derivative operator, $\alpha_i (i = 1, \dots, M_1)$ define the zeros of the filter, $\gamma_j (j = 1, \dots, M_2)$ represent the poles, I is the identity matrix and $M_1 > M_2$. Given the relationship between the activity-inducing and the innovation signal, the latter can be recovered as:

$$L\{x\}(t) = D\{s\}(t) = u(t) \quad (7)$$

where $L = DL_h$ and D is the derivative.

Therefore, for a given voxel, the neuronal-related signal could be estimated by solving the following regularized least-squares problem:

$$\hat{\mathbf{x}} = \arg \min_{\mathbf{x}} \frac{1}{2} \|\mathbf{y} - \mathbf{x}\|_2^2 + \Omega(\mathbf{x}), \quad (8)$$

where \mathbf{y} is the fMRI data and $\Omega(\mathbf{x})$ is the following l_1 -norm regularization term:

$$\hat{\mathbf{x}} = \arg \min_{\mathbf{x}} \frac{1}{2} \|\mathbf{y} - \mathbf{x}\|_2^2 + \lambda \|\Delta_L \{\mathbf{x}\}\|_1, \quad (9)$$

where λ is the regularization parameter.

This work evaluates the core of the two techniques, i.e., the regularized least-squares problem with temporal regularization, which corresponds to the generalized total-variation operator in Total Activation. Thus, we do not study the impact of spatial constraints, as we assume that spatial regularization terms should perform identically on both methods.

3. Methods

Simulations: In order to compare the two methods while controlling for their correct performance, we simulated a 400 seconds ($TR = 2$ s) activity-inducing signal with five neuronal events, convolved it with the canonical HRF, and we added noise of different sources (physiological, thermal, and motion-related) with different signal-to-noise ratios ($SNR = [20 \text{ dB}, 10 \text{ dB}, 3 \text{ dB}]$) that represent low, medium and high levels of noise as shown in Figure 1.

Motor task dataset: One healthy subject was scanned in a 3T MR scanner (Siemens) as part of a larger experiment under a Basque Center on Cognition, Brain and Language Review Board-approved protocol. T2*-weighted multi-echo fMRI data was acquired with a multiband (MB) multi-echo gradient echo-planar imaging sequence (340 scans, 52 slices, Partial-Fourier = 6/8, voxel size = 2.4x2.4x3 mm³, TR = 1.5 s, TEs = 10.6/28.69/46.78/64.87/82.96 ms, multiband factor = 4, flip angle = 70°, GRAPPA = 2). During the fMRI acquisition, subjects performed a motor task consisting of five different movements (left-hand finger tapping, right-hand finger tapping, moving the left toes, moving the right toes and moving the tongue). These conditions were randomly intermixed every 16 seconds, and were only repeated once the entire set of stimuli were presented. Data preprocessing consisted of optimally combining the echo time datasets, detrending of up to 5th-order Legendre polynomials, spatial smoothing (3 mm FWHM) and normalization to signal percentage change. For this comparison, we selected a voxel that best represented the right-hand finger-tapping paradigm based on a generalized linear model as shown in Figure 2.

Resting-state datasets: One healthy subject was scanned in a 3T MR scanner (Siemens) as part of a larger experiment under a Basque Center on Cognition, Brain

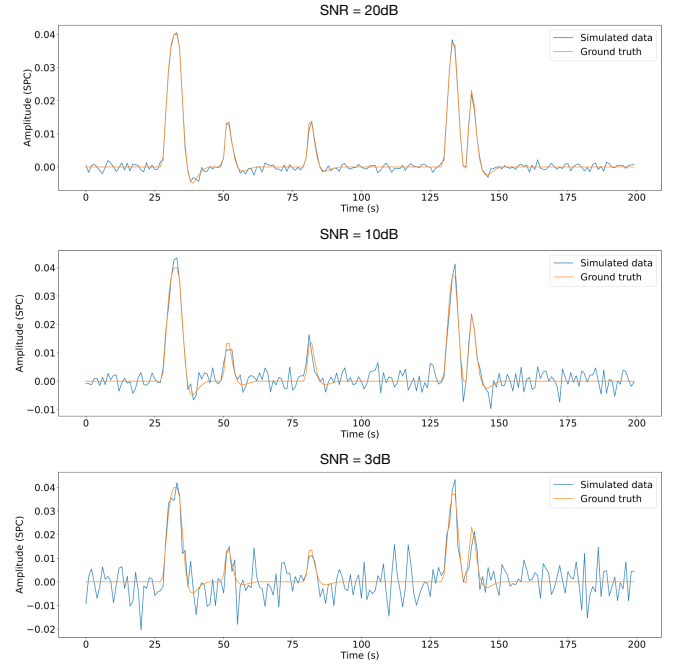


Figure 1: Simulated signal with different SNRs (20 dB, 10 dB and 3 dB).

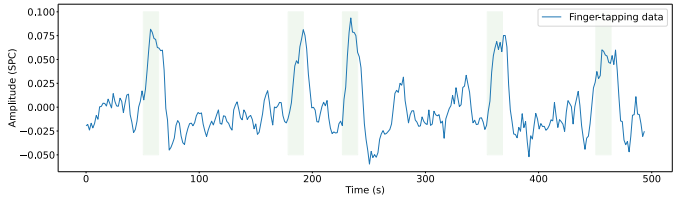


Figure 2: Most representative voxel of the finger-tapping task. Green blocks indicate the onsets and the duration of it.

and Language Review Board-approved protocol. Two runs of T2*-weighted fMRI data were acquired during resting-state, each with 10 min duration, with 1) a standard gradient-echo echo-planar imaging sequence (monoband) ($TR = 2000$ ms, $TE = 29$ ms, flip-angle = 78°, matrix size = 64x64, voxel size = 3x3x3 mm³, 33 axial slices with interleaved acquisition, slice gap = 0.6 mm) and 2) a simultaneous multislice gradient-echo echo-planar imaging sequence (multiband factor = 3) developed by the Center of Magnetic Resonance Research (University of Minnesota, USA; $TR = 800$ ms, $TE = 29$ ms, flip-angle = 60°, matrix size = 64×64, voxel size = 3x3x3 mm³, 42 axial slices with interleaved acquisition, no slice gap). Single-band reference images were also collected in both resting-state acquisitions for head motion realignment. During both acquisitions, participants were instructed to keep their eyes open, fixating a white cross that they saw through a mirror located on the head coil, and not to think about anything specific. Field maps were also obtained to correct for field distortions.

4. Results

A critical decision with deconvolution methods is the selection of the regularization parameter λ , for which many techniques have been proposed in the literature but an optimal is yet to be discovered. In fact, Paradigm Free Mapping and Total Activation base their selection of the regularization parameter on different criteria: the Bayesian Information Criterion (BIC) (Schwarz 1978) and Akaike Information Criterion (AIC) (Akaike 1998), and a selection based on the convergence of the residuals to a pre-estimated level of the noise, respectively. Hence, we compare the performance of the two algorithms with both selection criteria. Furthermore, we explore the differences between the techniques in terms of the estimation of the activity-inducing signal \mathbf{s} using the *spike model* in (3) and the innovation signal \mathbf{u} using the *block model* in (4).

4.1. Selection of the hemodynamic response function

With the aim of making a fair comparison of the two methods, we first compared their hemodynamic response functions. Figure 3A shows the difference in the hemodynamic response function that PFM and TA use by default for TR = 0.1 s and TR = 1 s adjusted to peak amplitude of one; i.e., the canonical HRF and the HRF resulting from the linear differential operator. The most observable difference between the two HRFs is the time to peak: the HRF used by Total Activation does not begin at zero while the one used by PFM does.

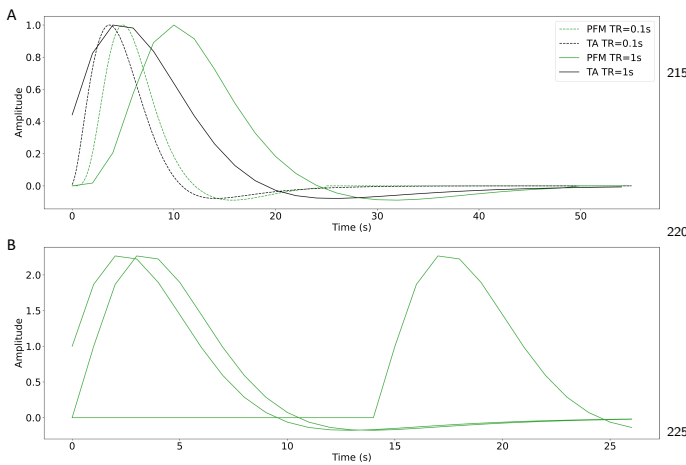


Figure 3: A) Canonical HRF models typically used by PFM (green) and TA (black) at TR = 0.1 s (dashed lines) and TR = 1 s (solid lines). Without loss of generality, the waveforms are scaled to unit amplitude for visualization. B) Representation of three shifted HRFs²³⁰ at TR=1 s (onsets=0, 1, and 15 s) that build the design matrix for PFM when the HRF model has been matched to that in TA.

While Paradigm Free Mapping allows for the use of any hemodynamic response function — the columns of the design matrix \mathbf{H} are composed by shifted versions of the HRF—the linear differential operator in TA is tailored for a fixed HRF. Hence, for practical reasons, we reproduced

the HRF in the Total Activation filter and incorporated it into the PFM formulation (Figure 3B).

4.2. Selection of the regularization parameter based on the estimation of the noise

Total Activation proposes to solve the inverse problem by updating the regularization parameter λ on every iteration n so that the residuals converge to a previously estimated noise level of the data fit $\tilde{\sigma}$, where this pre-estimated noise is calculated from the median absolute deviation of fine-scale wavelet coefficients (Daubechies, order 3) (Karahanoglu et al. 2013):

$$\lambda^{n+1} = \frac{N\tilde{\sigma}}{\frac{1}{2}\|\mathbf{y} - \mathbf{x}^n\|_F^2} \lambda^n. \quad (10)$$

Thus, we calculated the regularization path with PFM (as described in 4.3) and selected the λ corresponding to the residuals that were closest to the estimated noise level of the data. We applied Total Activation with temporal regularization in its original form. Figure 4 depicts the estimated activity-inducing, innovation, and activity-related signals when updating λ as in (10) in the three simulated SNR settings using the spike model (left) and the block model (right). Figure 4 (left) shows nearly identical results between PFM (left) and TA (right) with the use of the spike model. The minimal differences are the result of slight dissimilarities in the convergence of the residuals to the estimated noise level of the data. Likewise, the use of the block model with a selection of λ based on the MAD estimate of the noise yields results that are identical in practice as shown in Figure 4 (right).

In addition, we performed the same comparison on experimental data as introduced in 3. Figure 5 (row 3) illustrates that the estimated activity-inducing, innovation, and activity-related signals with PFM and TA are practically identical both for the spike model (left) and the block model (right).

4.3. Selection of the regularization parameter by solving the regularization path

Paradigm Free Mapping bases its selection of the regularization parameter on the Bayesian Information Criterion (BIC) and the Akaike Information Criterion (AIC). Hence, we calculated the regularization path with PFM by means of the least angle regression (LARS) algorithm (Efron et al. 2004) and used the λ s from the regularization path to solve the deconvolution problem with Total Activation.

Figure 6 (left) shows the regularization paths of PFM and TA side by side for the three SNR conditions for the spike model; i.e., the inverse problem described in (3). Each iteration of LARS reduces the value of λ ; i.e., reduces the sparsity promoted by the l_1 -norm, and reveals new non-zero coefficients as shown in the x axis of the heatmaps. Vertical black lines depict the selection of the regularization parameter based on BIC and AIC, and thus,

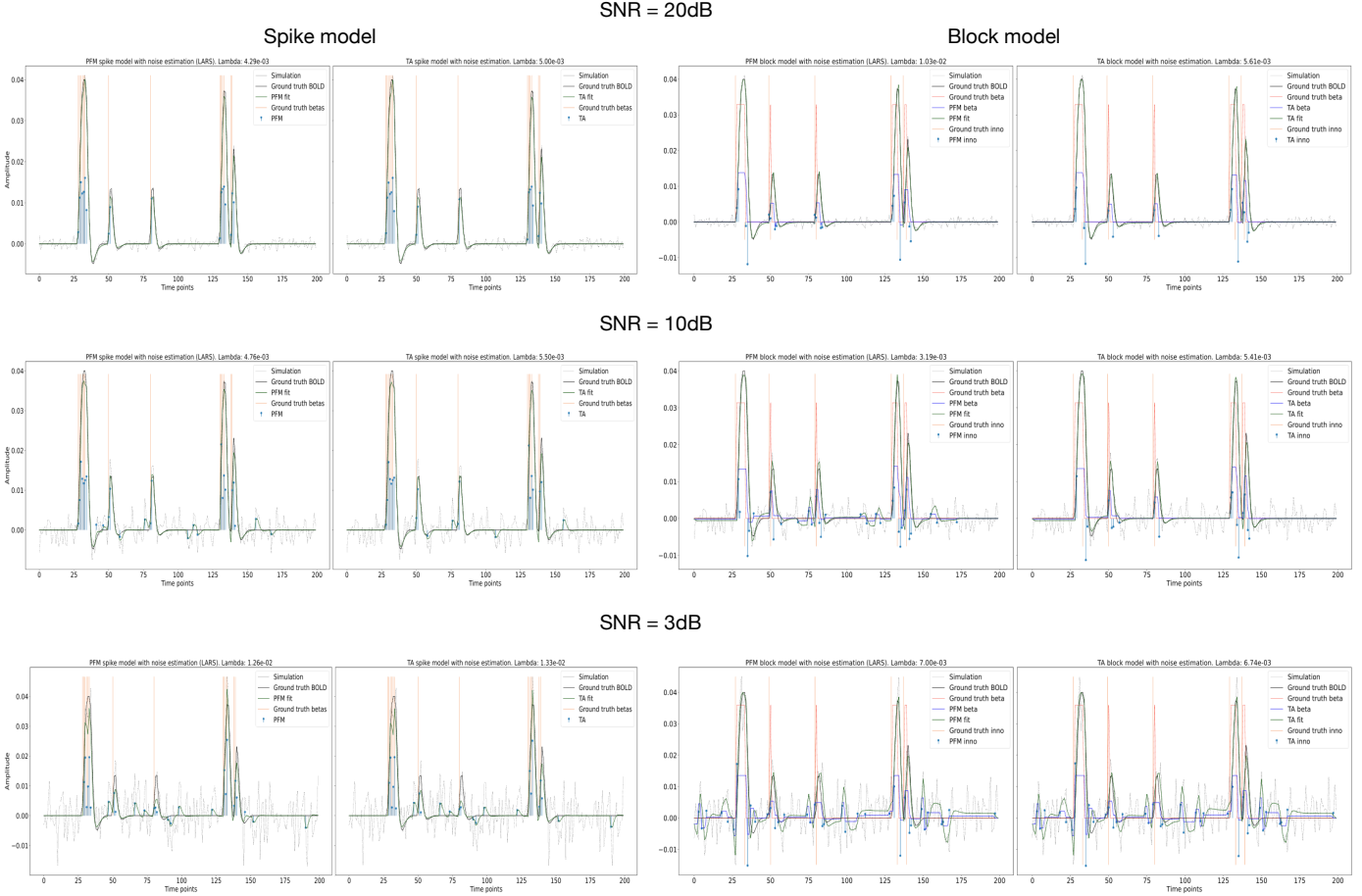


Figure 4: Estimated activity-inducing, innovation and activity-related (fit, \times) signals when λ is selected based on convergence of residuals to have same variance as MAD estimate of noise with spike model (left, with PFM on the left and TA on the right) and block model (right, with PFM on the left and TA on the right) on SNR = 20 dB (top), SNR = 10 dB (middle) and SNR = 3 dB (bottom).

the colored coefficients indicated by the vertical lines de-
260 depict the estimated activity-inducing signal $s(t)$. Figure 6
240 (right) illustrates the resulting estimation of the activity-
inducing and neuronal-related signals when basing the
selection of λ on BIC for the three simulated SNR
conditions. Given that the regularization paths of both tech-
265 niques are identical, the BIC-based selection of the reg-
ularization parameter and the results of deconvolving with
said λ are identical too (see Figure ??). Thus, Figure 6
demonstrates that, regardless of the simulated SNR condition,
270 both deconvolution algorithms produce identical reg-
ularization paths when the same HRF and regularization
parameters are applied, and hence, identical estimates of
the activity-inducing signal s and neuronal-related signal
x.

The regularization path to estimate innovation signals
275 yields mainly undistinguishable results for both PFM and
TA methods as shown in Figure 7 (left). Again, the BIC-
based selection of λ is identical for both PFM and TA, and
the estimation of the innovation signal u shows no distin-
guishable differences between the algorithms (see Figure 7

right). Therefore, both Paradigm Free Mapping and Total Activation yield nearly identical regularization paths and estimates of the innovation signal regardless of the simulated SNR condition when applying the same HRF and regularization parameters with the block model.

Furthermore, we performed the same analysis on experimental data as shown in Figure 5 (rows 1-2, 4). Row 1 demonstrates that the PFM and TA regularization paths are identical when deconvolving experimental data, regardless of the deconvolution model (spike or block). Even though tiny differences can be seen between the two methods in the BIC and AIC selection of λ in row 4, row 2 proves that the results are practically identical, and differences can be disregarded.

Additionally, in order to describe the extent of the discrepancies between the techniques, we calculated the residual sum of squares (RSS); i.e., the sum of squares of the differences between the estimated activity-inducing or innovation signals of PFM and TA as:

$$RSS = \frac{\sum (\hat{s}_{PFM} - \hat{s}_{TA})^2}{N} \quad (11)$$

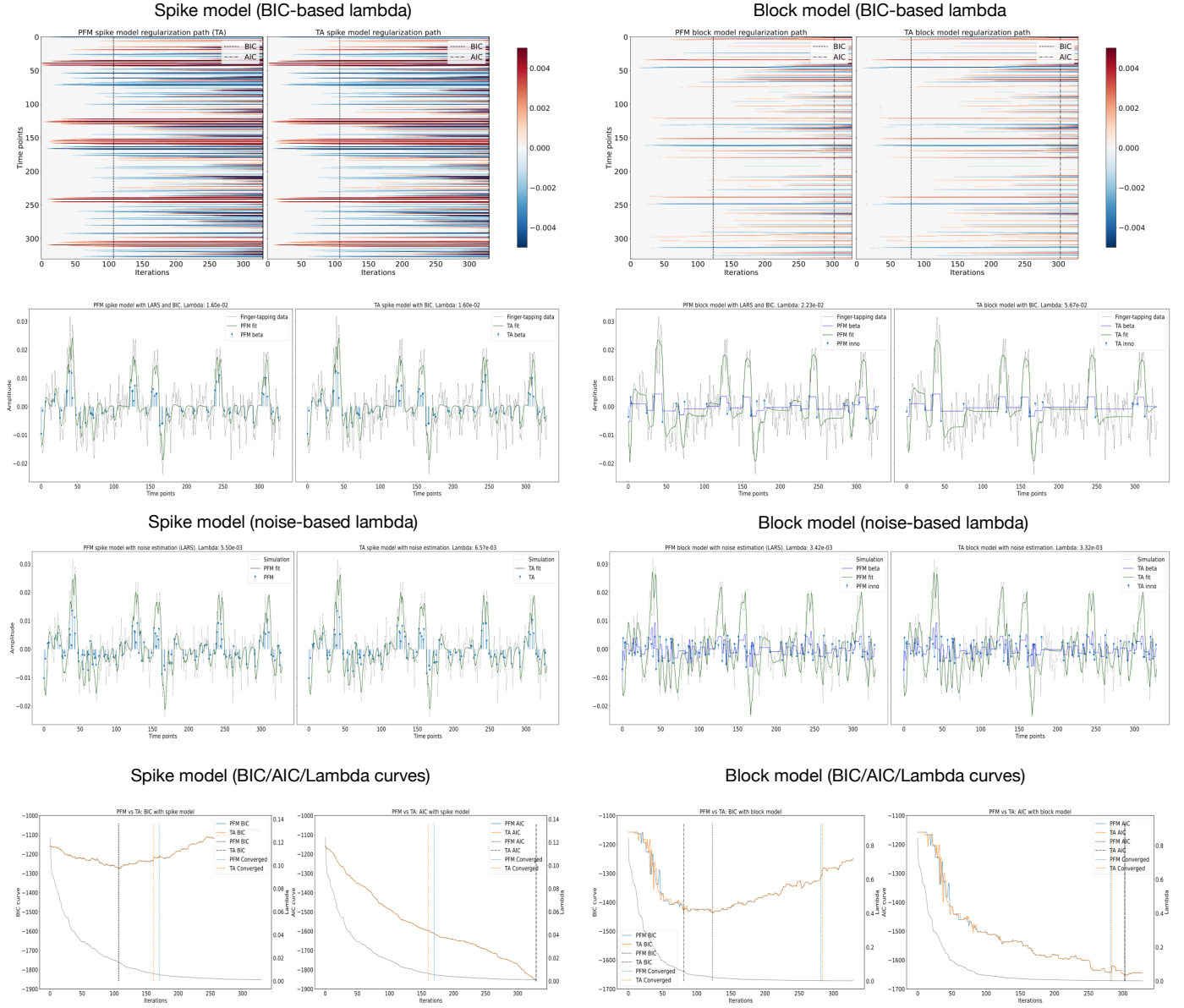


Figure 5: (Row 1) Regularization paths of the estimated activity-inducing signal (spike model — left) and innovation signal (block model — right); (Row 2) activity-inducing, innovation and activity-related (fit, \mathbf{x}) signals when λ is selected based on BIC, or (Row 3) based on convergence of residuals to have same variance as MAD estimate of noise; (Row 4) Corresponding cost curves of BIC and AIC. The vertical lines indicate the three options to select λ (BIC, AIC and Converged/MAD).

Figure 8 depicts the RSS of the spike (Figure 8A) and block (Figure 8B) models for the three experimental datasets introduced: i.e., motor, monoband and multi-band. It is clear that RSS values are lower than those of the activity-inducing and innovation signals, suggesting that the differences between Paradigm Free Mapping and Total Activation are negligible.

5. Discussion

This work demonstrates that Paradigm Free Mapping and Total Activation yield practically identical results when

the same HRF model and regularization parameter are employed, demonstrating that synthesis and analysis models are equivalent for temporal fMRI deconvolution. Thus, previously observed differences in performance must be due to differences in usage options. With the equivalence in the temporal deconvolution demonstrated, it is reasonable to assume that additional regularization terms in the spatial or temporal domains would not modify this equivalence when convex operators are employed; e.g., when the regularization problem can be solved by means of the Fast Iterative Shrinkage-Thresholding Algorithm (FISTA)

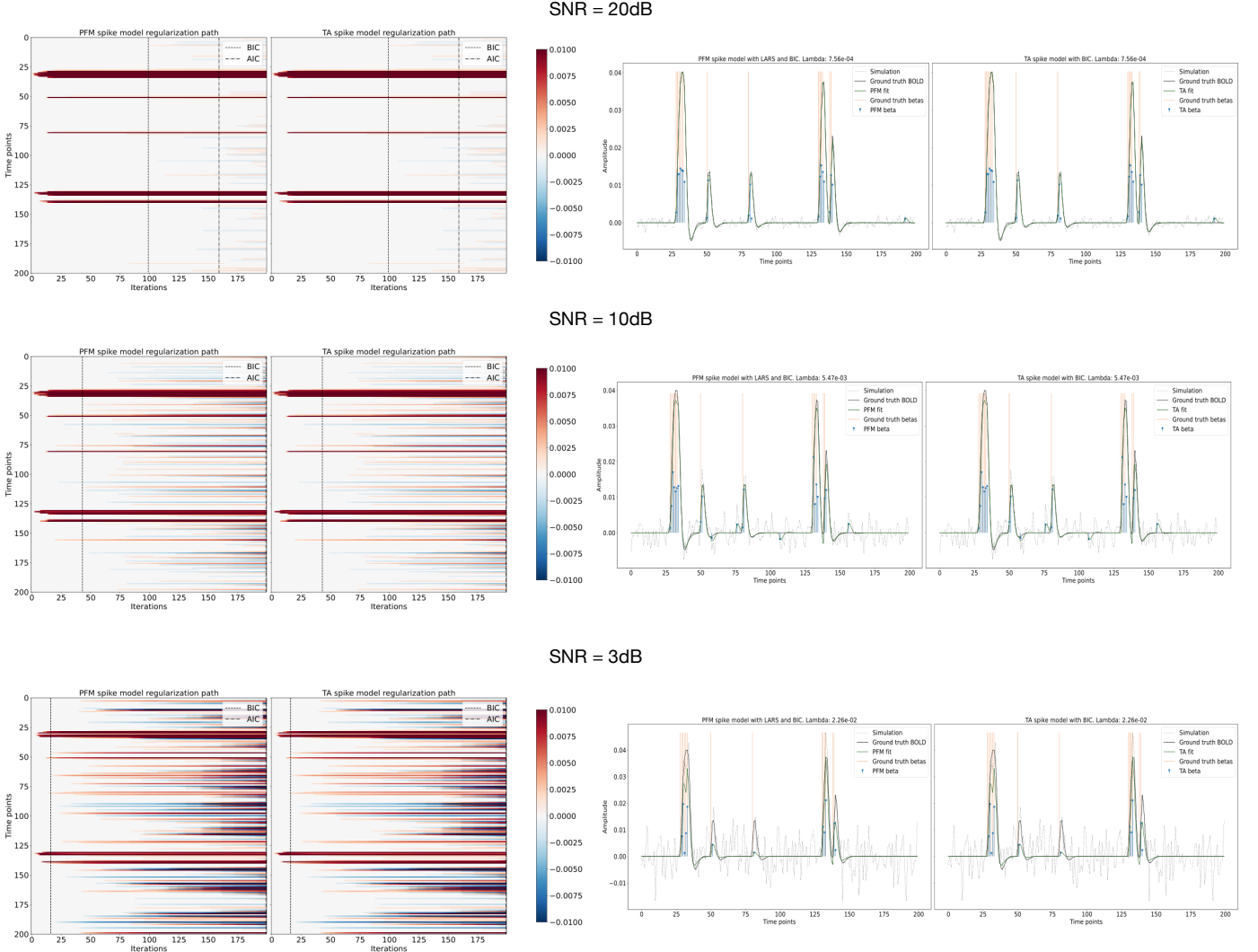


Figure 6: Spike model simulations. (Left) Heatmap of the regularization paths of the activity-inducing signal estimated with PFM and TA as a function of λ (increasing number of iterations in x-axis), whereas each row in the y-axis shows one time-point. Vertical lines denote iterations corresponding to the Akaike and Bayesian Information Criteria (AIC and BIC) optima. (Right) Estimated activity-inducing (blue) and activity-related (green) signals when set based on BIC. All estimates are identical, regardless of SNR.

(Beck and Teboulle 2009) or the Generalized Forward-₃₁₀ Backward Splitting (Raguet et al. 2013) techniques. Our findings are in line with the equivalence of analysis and synthesis methods in under-determined cases ($N \leq V$) as demonstrated in (Elad et al. 2007).

Taking into account the advantages and disadvantages of the presented techniques shown in Table 1, future work will improve and extend deconvolution methods for fMRI.₃₁₅ For instance, the appropriate formulation depending on data acquisition (i.e., single-echo vs multi-echo) could be studied and compared with existing methods (Caballero-Gaudes et al. 2019), or formulations that account for HRF variability could be investigated too (Badillo et al. 2013; Gaudes et al. 2012; Farouj et al. 2019). Furthermore, robust methods to select the regularization parameter (Uruñuela

et al. 2020; Meinshausen and Bühlmann 2010) and other potential $\ell_{p,q}$ -norm regularization terms (e.g., $p < 1$) or debiasing approaches could be explored.

6. Code availability

The code and materials used in this work can be found in the following GitHub repository: https://github.com/eurunuela/pfm_vs_ta. We encourage the reader to play with the parameters (e.g. SNR, varying HRF options and mismatch between algorithms, TR, number of events, onsets, and durations) in the provided Jupyter notebooks.

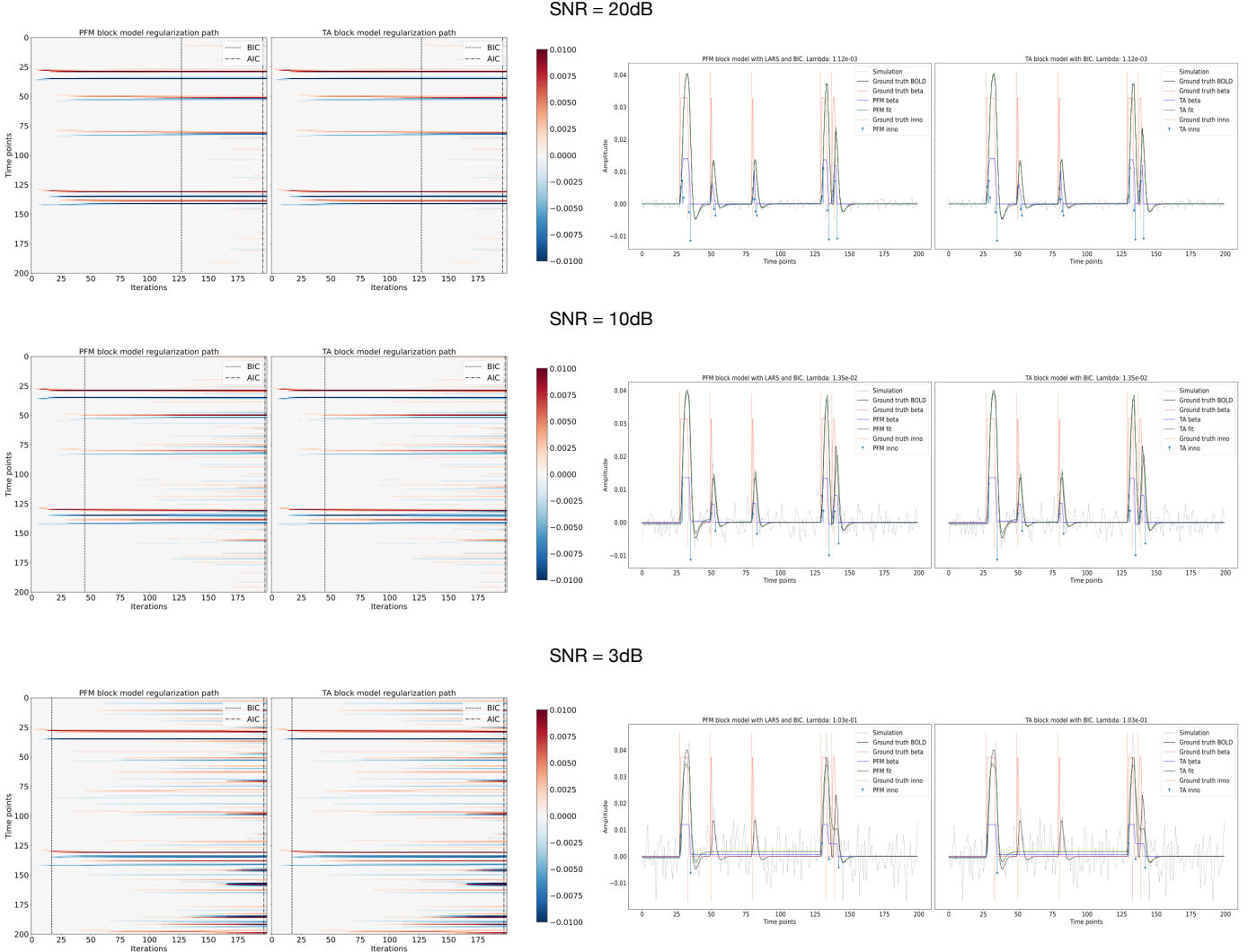


Figure 7: Block model simulations. (Left) Heatmap of the regularization paths of the innovation signal estimated with PFM and TA as a function of λ (increasing number of iterations in x-axis), whereas each row in the y-axis illustrates one time-point. Vertical lines denote iterations corresponding to the Akaike and Bayesian Information Criteria (AIC and BIC) optima. (Right) Estimated innovation (blue) and activity-related (green) signals when λ is set based on BIC. All the estimates are identical when compared between the PFM and TA cases, regardless of SNR.

320 7. Acknowledgements

This research was funded by the European Union's Horizon 2020 research and innovation program (agreement No. 713673 of the Marie Skłodowska-Curie grant), La Caixa Foundation (ID 100010434, fellowship code LCF/B₃₂₅Q/IN17/11620063), the Spanish Ministry of Economy and Competitiveness (RYC-2017-21845), the Basque Government (BERC 2018-2021, PIBA_2019_104, PRE_2019_1_0054), and the Spanish Ministry of Science, Innovation and Universities (PID2019-105520GB-100).

330 References

- Akaike, H., 1998. Information Theory and an Extension of the Maximum Likelihood Principle, in: Parzen, E., Tanabe, K., Kitagawa, G. (Eds.), Selected Papers of Hirotugu Akaike. Springer, New York, NY. Springer Series in Statistics, pp. 199–213. doi:10.1007/978-1-4612-1694-0_15.
- Allan, T.W., Francis, S.T., Caballero-Gaudes, C., Morris, P.G., Liddle, E.B., Liddle, P.F., Brookes, M.J., Gowland, P.A., 2015. Functional connectivity in mri is driven by spontaneous bold events. *PloS one* 10, e0124577.
- Badillo, S., Vincent, T., Ciuci, P., 2013. Group-level impacts of within-and between-subject hemodynamic variability in fmri. *Neuroimage* 82, 433–448.
- Beck, A., Teboulle, M., 2009. A fast iterative shrinkage-thresholding algorithm. *Society for Industrial and Applied Mathematics Journal on Imaging Sciences* 2, 183–202. doi:10.1137/080716542.
- Betzel, R.F., Byrge, L., Esfahlani, F.Z., Kennedy, D.P., 2020.

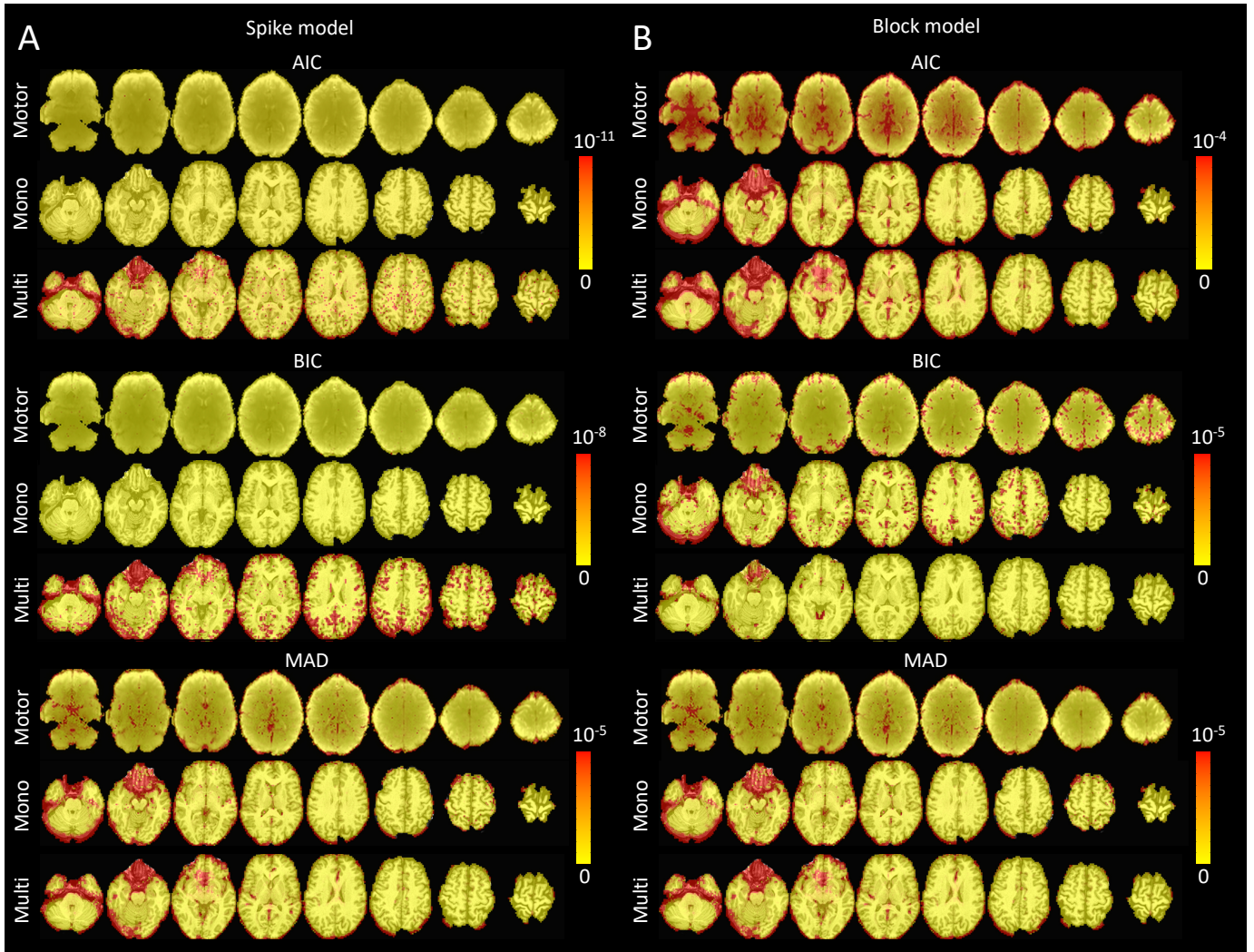


Figure 8: Sum of squares of the differences of the activity-inducing signals estimated with Paradigm Free Mapping and Total activation for the different selections of the regularization parameter: AIC (top), BIC (middle), and MAD (bottom). The sum of square difference maps are shown for the three experimental datasets introduced in Section 3: the motor task (Motor), the monoband resting-state (Mono), and the multiband resting-state (Multi) datasets. A) Sum of squares of the differences when using the spike model. B) Sum of squares of the differences when using the block model.

- Temporal fluctuations in the brain's modular architecture during movie-watching. *NeuroImage* 213, 116687. doi:10.1016/j.neuroimage.2020.116687.
- Bommarito, G., Tarun, A., Farouj, Y., Preti, M.G., Petracca, M.,³⁷⁰ Droby, A., El Mendili, M.M., Inglese, M., Van De Ville, D., 2020. Functional network dynamics in progressive multiple sclerosis. medRxiv .
- Bruckstein, A.M., Donoho, D.L., Elad, M., 2009. From Sparse Solutions of Systems of Equations to Sparse Modeling of Signals and³⁷⁵ Images. *SIAM Review* 51, 34–81. doi:10.1137/060657704.
- Caballero-Gaudes, C., Moia, S., Panwar, P., Bandettini, P.A., Gonzalez-Castillo, J., 2019. A deconvolution algorithm for multi-echo functional mri: Multi-echo sparse paradigm free mapping.³⁸⁰ *NeuroImage* 202, 116081.
- Caballero Gaudes, C., Petridou, N., Francis, S.T., Dryden, I.L., Gowland, P.A., 2013. Paradigm free mapping with sparse regression automatically detects single-trial functional magnetic resonance imaging blood oxygenation level dependent responses. *Human Brain Mapping* doi:10.1002/hbm.21452.
- Cherkaoui, H., Moreau, T., Halimi, A., Ciuciu, P., 2019. Sparsity-based Blind Deconvolution of Neural Activation Signal in fMRI, in: ICASSP 2019 - 2019 IEEE International Conference on Acoustics, Speech and Signal Processing (ICASSP), pp. 1323–1327. doi:10.1109/ICASSP.2019.8683358.
- Cifre, I., Flores, M.T.M., Ochab, J.K., Chialvo, D.R., 2020a. Revisiting non-linear functional brain co-activations: directed, dynamic and delayed. arXiv preprint arXiv:2007.15728 .
- Cifre, I., Zarepour, M., Horovitz, S., Cannas, S., Chialvo, D., 2020b. Further results on why a point process is effective for estimating correlation between brain regions. *Papers in Physics* 12, 120003–120003.
- Efron, B., Hastie, T., Johnstone, I., Tibshirani, R., 2004. Least Angle Regression. *The Annals of Statistics* 32, 407–499. doi:10.1214/009053604000000067.
- Elad, M., Milanfar, P., Rubinstein, R., 2007. Analysis versus synthesis in signal priors. *Inverse problems* 23, 947.
- Esfahlani, F.Z., Jo, Y., Faskowitz, J., Byrge, L., Kennedy, D.P., Sporns, O., Betzel, R.F., 2020. High-amplitude fluctuations in cortical activity drive functional connectivity. *Proceedings of the National Academy of Sciences* 117, 28393–28401.

Paradigm Free Mapping	Total Activation
+ Its formulation can be extended straightforwardly for deconvolution of multiple signals with a common neuronal-related signal, e.g., for multi-echo formulations Caballero-Gaudes et al. 2019.	
+ The model can implement any HRF shape very easily since it only requires the coefficients at the required temporal resolution.	-
-	-

Table 1: Advantages (+) and disadvantages (-) of Paradigm Free Mapping and Total Activation with respect to each other.

- temporal regularization. *NeuroImage* doi:10.1016/j.neuroimage.2013.01.067.
- Karahanoğlu, F.I., Van De Ville, D., 2015. Transient brain activity disentangles fMRI resting-state dynamics in terms of spatially and temporally overlapping networks. *Nature Communications* 6, 7751. doi:10.1038/ncomms8751.
- Karahanoğlu, F.I., Van De Ville, D., 2017. Dynamics of large-scale fMRI networks: Deconstruct brain activity to build better models of brain function. *Current Opinion in Biomedical Engineering* 3, 28–36. doi:10.1016/j.cobme.2017.09.008.
- Khalidov, I., Fadili, J., Lazeyras, F., Van De Ville, D., Unser, M., 2011. Activelets: Wavelets for sparse representation of hemodynamic responses. *Signal processing* 91, 2810–2821.
- Kinany, N., Pirondini, E., Micera, S., Van De Ville, D., 2020. Dynamic Functional Connectivity of Resting-State Spinal Cord fMRI Reveals Fine-Grained Intrinsic Architecture. *Neuron* 108, 424–435.e4. doi:10.1016/j.neuron.2020.07.024.
- Liu, X., Chang, C., Duyn, J.H., 2013. Decomposition of spontaneous brain activity into distinct fmri co-activation patterns. *Frontiers in systems neuroscience* 7, 101.
- Liu, X., Duyn, J.H., 2013. Time-varying functional network information extracted from brief instances of spontaneous brain activity. *Proceedings of the National Academy of Sciences* 110, 4392–4397.
- Liu, X., Zhang, N., Chang, C., Duyn, J.H., 2018. Co-activation patterns in resting-state fmri signals. *Neuroimage* 180, 485–494.
- Lopes, R., Lina, J.M., Fahoum, F., Gotman, J., 2012. Detection of epileptic activity in fmri without recording the eeg. *Neuroimage* 60, 1867–1879.
- Majeed, W., Magnuson, M., Hasenkamp, W., Schwab, H., Schumacher, E.H., Barsalou, L., Keilholz, S.D., 2011. Spatiotemporal dynamics of low frequency bold fluctuations in rats and humans. *Neuroimage* 54, 1140–1150.
- Majeed, W., Magnuson, M., Keilholz, S.D., 2009. Spatiotemporal dynamics of low frequency fluctuations in bold fmri of the rat. *Journal of Magnetic Resonance Imaging: An Official Journal of the International Society for Magnetic Resonance in Medicine* 30, 384–393.
- Meinshausen, N., Bühlmann, P., 2010. Stability selection. *Journal of the Royal Statistical Society: Series B (Statistical Methodology)* 72, 417–473.
- Petridou, N., Gaudes, C.C., Dryden, I.L., Francis, S.T., Gowland, P.A., 2013. Periods of rest in fMRI contain individual spontaneous events which are related to slowly fluctuating spontaneous activity. *Human Brain Mapping* 34, 1319–1329. doi:10.1002/hbm.21513.
- Raguet, H., Fadili, J., Peyré, G., 2013. A Generalized Forward-Backward Splitting. *SIAM Journal on Imaging Sciences* 6, 1199–1226. doi:10.1137/120872802.
- Schwarz, G., 1978. Estimating the Dimension of a Model. *Annals of Statistics* 6, 461–464. doi:10.1214/aos/1176344136.
- Shine, J.M., Bissett, P.G., Bell, P.T., Koyejo, O., Balsters, J.H., Gorgolewski, K.J., Moodie, C.A., Poldrack, R.A., 2016. The dynamics of functional brain networks: integrated network states during cognitive task performance. *Neuron* 92, 544–554.
- Shine, J.M., Koyejo, O., Bell, P.T., Gorgolewski, K.J., Gilat, M., Poldrack, R.A., 2015. Estimation of dynamic functional connectivity using multiplication of temporal derivatives. *NeuroImage* 122, 399–407.
- Tarun, A., Wainstein-Andriano, D., Sterpenich, V., Bayer, L., Perogamvros, L., Solms, M., Axmacher, N., Schwartz, S., Van De Ville, D., 2020. Nrem sleep stages specifically alter dynamical integration of large-scale brain networks. *Iscience* 24, 101923.
- Tibshirani, R., 1996. Regression Shrinkage and Selection Via the Lasso. *Journal of the Royal Statistical Society: Series B (Methodological)* 58, 267–288. doi:10.1111/j.2517-6161.1996.tb02080.x.
- Uruñuela, E., Jones, S., Crawford, A., Shin, W., Oh, S., Lowe, M., Caballero-Gaudes, C., 2020. Stability-Based Sparse Paradigm Free Mapping Algorithm for Deconvolution of Functional MRI Data. *Proceedings of the Annual International Conference of the IEEE Engineering in Medicine and Biology Society, EMBS 2020-July*, 1092–1095. doi:10.1109/EMBC44109.2020.9176137.
- Zhang, X., Pan, W.J., Keilholz, S.D., 2020. The relationship between

bold and neural activity arises from temporally sparse events.
Neuroimage 207, 116390.

- 495 Zöller, D., Sandini, C., Karahanoglu, F.I., Padula, M.C., Schaer,
M., Eliez, S., Van De Ville, D., 2019. Large-scale brain network
dynamics provide a measure of psychosis and anxiety in 22q11.2
deletion syndrome. *Biological Psychiatry: Cognitive Neuroscience
and Neuroimaging* 4, 881–892.